

Stem cell dynamics and cellular heterogeneity across lineage subtypes of castrate-resistant prostate cancer

Michael L Beshiri, Brian J Capaldo, Ross Lake, Anson T Ku, Danielle Burner, Caitlin M Tice, Crystal Tran, Julianna Kostas, Aian Neil Alilin, JuanJuan Yin, Supreet Agarwal, Samantha A Morris, Fatima H Karzai, Tamara L Lotan, William L Dahut, Adam G Sowalsky, Kathleen Kelly







The advertisement banner features a dark blue background on the left with a white laboratory refrigerator. The text "You Don't Need Reproducible Research UNTIL YOU DO." is displayed in white and green. Below this, a green bar contains the text "Minimize uncertainty with PHCbi brand products" in white. The PHCbi logo, consisting of the letters "phc" in blue and "bi" in red, is positioned on the right side of the banner.

You Don't Need Reproducible Research
UNTIL YOU DO.
Minimize uncertainty with PHCbi brand products

phcbi

Stem cell dynamics and cellular heterogeneity across lineage subtypes of castrate-resistant prostate cancer

Michael L. Beshiri¹, Brian J. Capaldo¹, Ross Lake^{1, }, Anson T. Ku^{1, }, Danielle Burner¹, Caitlin M. Tice¹, Crystal Tran¹, Julianna Kostas¹, Aian Neil Alilin¹, JuanJuan Yin¹, Supreet Agarwal¹, Samantha A. Morris^{2,3,4}, Fatima H. Karzai⁵, Tamara L. Lotan⁶, William L. Dahut^{5, }, Adam G. Sowalsky^{1, }, Kathleen Kelly^{*,1}

¹Laboratory of Genitourinary Cancer Pathogenesis, Center for Cancer Research, National Cancer Institute, NIH, Bethesda, MD, United States,

²Department of Developmental Biology, Washington University School of Medicine in St Louis, St Louis, MO, United States,

³Department of Genetics, Washington University School of Medicine in St Louis, St Louis, MO, United States,

⁴Center of Regenerative Medicine, Washington University School of Medicine in St Louis, St Louis, MO, United States,

⁵Genitourinary Malignancies Branch, National Cancer Institute, NIH, Bethesda, MD, United States,

⁶Department of Pathology, Johns Hopkins University School of Medicine, Baltimore, MD, United States

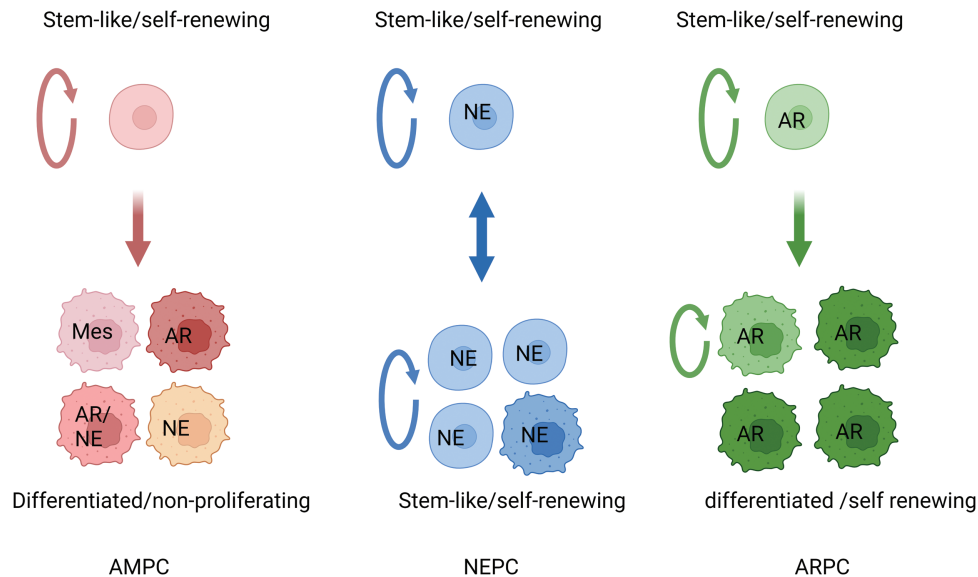
*Corresponding author: Kathleen Kelly, Laboratory of Genitourinary Cancer Pathogenesis, Center for Cancer Research, National Cancer Institute, NIH, Building 37 Room 1066, Bethesda MD 20878 (kellyka@mail.nih.gov).

Abstract

To resist lineage-dependent therapies such as androgen receptor inhibition, prostate luminal epithelial adenocarcinoma cells often adopt a stem-like state resulting in lineage plasticity and phenotypic heterogeneity. Castrate-resistant prostate adenocarcinoma can transition to neuroendocrine (NE) and occasionally to amphicrine, co-expressed luminal and NE, phenotypes. We developed castrate-resistant prostate cancer (CRPC) patient-derived organoid models that preserve heterogeneity of the originating tumor, including an amphicrine model displaying a range of luminal and NE phenotypes. To gain biological insight and to identify potential treatment targets within heterogeneous tumor cell populations, we assessed the lineage hierarchy and molecular characteristics of various CRPC tumor subpopulations. Transcriptionally similar stem/progenitor (St/Pr) cells were identified for all lineage populations. Lineage tracing in amphicrine CRPC showed that heterogeneity originated from distinct subclones of infrequent St/Pr cells that produced mainly quiescent differentiated amphicrine progeny. By contrast, adenocarcinoma CRPC progeny originated from St/Pr cells and self-renewing differentiated luminal cells. Neuroendocrine prostate cancer (NEPC) was composed almost exclusively of self-renewing St/Pr cells. Amphicrine subpopulations were enriched for secretory luminal, mesenchymal, and enzalutamide treatment persistent signatures that characterize clinical progression. Finally, the amphicrine St/Pr subpopulation was specifically depleted with an AURKA inhibitor, which blocked tumor growth. These data illuminate distinct stem cell (SC) characteristics for subtype-specific CRPC in addition to demonstrating a context for targeting differentiation-competent prostate SCs.

Key words: prostate cancer; cancer stem cells; clinical translation; progenitor cells; self-renewal; amphicrine; drug target.

Graphical Abstract



Significance Statement

For advanced prostate cancer, therapeutic resistance to androgen signaling suppression increasingly involves the development of lineage plasticity. The cellular states of transition and subpopulation heterogeneity that underlie lineage plasticity are not well understood, which is an ongoing challenge to the design of effective treatments. Using patient-derived organoid models of various castrate-resistant prostate cancer (CRPC) lineage subtypes, we observed distinct patterns with respect to stem/progenitor (St/Pr) activity and associated growth phenotypes. The simultaneous expression of androgen receptor (AR-driven and neuroendocrine identities, so-called amphicrine tumors, is thought to be an early dedifferentiation stage in plasticity-mediated resistance. We observed in an amphicrine model of CRPC that a rare but necessary bipotent St/Pr population is suppressed by AURKA inhibitors, leading to tumor regression, while adenocarcinoma demonstrates both self-renewing differentiated luminal cells and St/Pr. These data suggest that AURKA inhibition may block the amplification of a resistance dedifferentiation pathway and should be considered in combination with AR signaling inhibitors for adenocarcinoma with characteristics of lineage plasticity.

Introduction

Targeted therapies are designed to attack cancer cells through specific molecular pathways to maximize impact and minimize general toxicity to the patient. Cancer cells can develop resistance to targeted therapies through a process of trans-differentiation where drug-sensitive tumor cells modify their lineage to acquire an alternate cellular identity that is not dependent on the targeted pathway for survival.^{1,3} Transition from an adenocarcinoma (ARPC) to neuroendocrine (NE) lineage is one differentiation path taken in various epithelial cancers including lung and prostate (denoted ARPC for prostate adenocarcinoma).^{1,4} In metastatic castration-resistant prostate cancer (mCRPC), a decrease in luminal epithelial identity upon treatment with potent AR pathway inhibitors occurs in ~20% of cases.^{1,5,6} Acquisition of a less differentiated, stem-like state leads to a spectrum of mCRPC phenotypes, termed lineage plasticity, which appears to exist along a continuum.⁷ A detailed characterization of stem-like cells across various models representative of heterogeneous CRPC is needed to gain insight into the process and to identify cellular points of therapeutic vulnerability. The stages of lineage plasticity most proximal to ARPC are thought to be CRPC with low AR signaling as well as CRPC representing an adenocarcinoma lineage that gains NE features while maintaining AR activity, so-called amphicrine) subtype (denoted AMPC).⁷ The transition to highly aggressive

small-cell neuroendocrine prostate cancer (scNEPC) or a mesenchymal/basal AR⁺NE⁻ phenotype is thought to often proceed via clonal selection following the loss of *RB1* and/or *TP53* function.²

Because prostate cancer does not readily establish in culture, a large share of research historically has relied on clinical samples and a relatively small number of cell lines, limiting investigations into the origins of phenotypic tumor heterogeneity.⁸ The use of organoid culturing procedures has allowed the establishment of new models derived from contemporary patient samples.⁸ We established and characterized an amphicrine biopsy-derived CRPC organoid model harboring mutations in *ARID1A* and *ARID1B*. Amphicrine CRPC has been increasingly recognized in clinical samples, although an amphicrine model originating from a pathologically validated patient sample is not in common use.⁷ We describe a tractable model that has captured the phenotypic heterogeneity documented in the originating patient samples and provides a clinically relevant model to study the dynamic interrelation of the ARPC and NE lineage states.

ARID1A and *ARID1B* are mutually exclusive members of the cBAF complex, and *ARID1A* is mutated in ~20% of cancers. BAF (Brahma associated factor, also known as SWI/SNF) complexes remodel chromatin structure, positively or negatively regulating gene expression.⁹ Mistargeting of BAF complexes by disease-relevant transcription

factors (TFs) contributes to loss of tumor suppression and context-dependent abnormal differentiation.^{10,11} *ARID1A* mutations in breast cancer determine resistance to estrogen receptor (ER)-targeted therapy by promoting cellular plasticity resulting from loss of chromatin interactions for luminal lineage-determining TFs such as ER, FOXA1, and GATA3.^{12,13} In addition, *ARID1A* mutations occur with increased frequency relative to adenocarcinomas in NE breast cancers¹⁴ and are considered drivers for some NE tumors, including gastrointestinal NETs and pulmonary carcinoids.^{15,16} These data suggest the hypothesis that epigenetic deregulation of transformation is one mechanism associated with differentiated NE tumors. By contrast, small-cell NE tumors are driven mechanistically by *RB1* and *TP53* pathway mutations.

Using lineage tracing, we experimentally determined the proliferative and differentiated status of subpopulations across ARPC, NEPC, and AMPC organoid subtypes. Following integration of single-cell RNA sequencing (scRNAseq) clusters across multiple models, we observed the existence of a common stem/progenitor (St/Pr) cell phenotype consistently present in all models, which is rare among AMPC and ARPC and frequent in scNEPC models. In ARPC, there is a unique population of dividing, differentiated cells, while differentiated amphoteric cells are not self-sustaining but are continuously generated from progenitors. Subpopulations of amphoteric cells encompass gene signatures that characterize progressive phenotypes in clinical samples. Finally, we show that inhibition of St/Pr cells is sufficient to inhibit the growth of patient-derived AMPC.

Results

Patient-derived organoids with mutations in BAF core complex components demonstrate lineage plasticity and NE differentiation

We established a set of patient-derived organoid models designated NCI-PC35-1 and NCI-PC35-2¹⁷ (PC35-1 and PC35-2) from 2 spatially separated needle biopsies of an mCRPC lymph node metastasis that was histologically ARPC with islands of NE marker-expressing cells (Figure 1A, 1B; Supplementary Figure S1A). There was no evidence of NE markers in the primary tumor (Supplementary Figure S1B). Whole-genome sequencing (WGS) phylogenetic analysis revealed that PC35-1 and PC35-2 arose from a common ancestor in the primary tumor featuring genomic mutations with high oncogenic potential: a deep deletion of *CDKN1B*, a frameshift mutation of *ARID1A* and a small deletion in *ARID1B* (Supplementary Figure S2A, S2B). *ARID1A/B* are core components of the BAF complex, and reductions of *ARID1A* and *ARID1B* have been shown to drive carcinogenesis and neural developmental disorders.^{18,19} The *RB1*, *TP53*, and *PTEN* loci were intact and expressed (Supplementary Figure S2C). Phylogenetic analysis showed little geographic co-mingling of PC35-1 and PC35-2, which demonstrated 77% and 97% exclusive subclonal genomic variants, respectively. Thus, the 2 PC35 models shared driver mutations and similar phenotypes but represented divergent clonal populations from separated core biopsies within the heterogeneous tumor. No additional known driver mutations were found in the metastatic clones except for a tandem duplication of the AR enhancer, a frequent genomic event in CRPC (Supplementary Figure S2D), suggesting that the

primary tumor had high metastatic potential. An analysis of prostate cancer cohorts in cBioportal and WCDT data sets revealed that *ARID1A* and *ARID1B* mutations occur at a frequency of ~1% and ~2% and demonstrate enrichment to ~6% and 15%, respectively, in the CRPC setting, consistent with promotion of androgen resistance (Supplementary Figure S2E).

The organoids reflected the pathology of the metastatic tumor with a range of AR and/or NE-marked populations (Figure 1B, 1D). All possible combinations of AR and NE marker (CHGA) expression status were observed in individual cells. Furthermore, mapping AR activity and NE signature scores of bulk RNAseq data relative to other ARPC and NEPC models and clinical samples placed PC35-1/2 at the NEPC-adjacent edge of the ARPC cluster, consistent with the pathology and an early evolutionary step in ARPC lineage switching (Figure 1E). The distribution of phenotypic markers was stable over time (Supplementary Figure S3A). EdU labeling and growth kinetic experiments showed that a minor population of PC35-1/2 cells underwent multiple divisions while the majority of cells were not proliferative (Figure 1F; Supplementary Figure 3B, 3C). This stands in contrast to scNEPC and ARPC organoid models, where a majority of the cells are proliferative (Supplementary Figure S3C).

Single-cell RNAseq reveals subclonal heterogeneity and lineage gradients

To better understand the heterogeneity and subpopulation dynamics of the organoid models, we performed scRNAseq. By this method, we identified 2 major clusters (I and II) in PC35-1 and 3 (I, II, and III) in PC35-2, with a heterogeneous range of lineage phenotypes (Figure 2A). Clusters were designated by phenotype based on AR, NE, and proliferation (PRLF) signature scores (Figure 2B, 2D; Supplementary Figure S4) as well as by comparison to a variety of phenotypically and biologically defined signatures for prostate cancer models, presented subsequently in Figure 4; Supplementary Figure S9. Additionally, we performed RNA velocity analysis²⁰ on the data to infer temporal states of differentiation (Supplementary Figure S5). St/Pr cells, which separated into 2 subclusters characteristic of the stem (red) and transit-amplifying (blue) cells, were designated based upon a high proliferation score, enrichment of stem marker gene expression, long RNA velocity vectors showing a multidirectional pattern (Supplementary Figure S5), and a prominent G2/M transcriptional profile (Supplementary Figure S4D). Prominent in both PC35-1 and PC35-2 was an amphoteric population (colored orange) demonstrating features of both AR- and NE- gene expression, a low proliferation score, and a uniform direction of short RNA velocity vectors. Amphoteric populations demonstrated gradients of AR and NE-dependent gene expression (Supplementary Figure S4B, S4C). In addition, PC35-2 had 2 additional ARPC clusters, one enriched for *NR3C1*-dependent transcription, and PC35-1 had an additional mesenchymal cluster. In contrast to PC35-1/2, the ARPC model PC44 and NEPC model LuCaP 145.2 were homogenous in their respective lineages and PRLF scores, indicating a more equal proliferative potential for the majority of cells in the population (Figure 2B, 2D). In summary, heterogeneity of PC35-1/2 captured from the patient tumor includes both inter- and intra-cluster lineage plasticity.

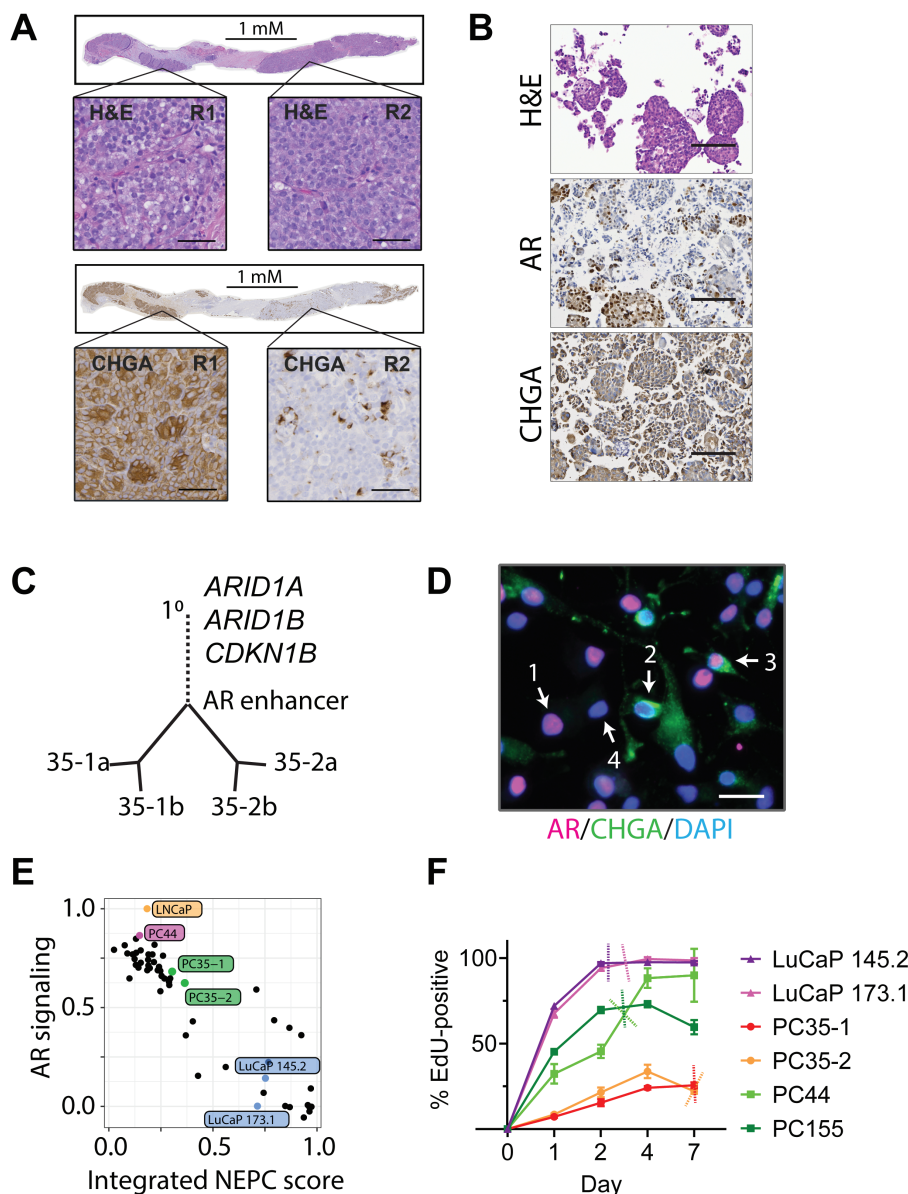


Figure 1. Patient-derived organoid models of mCRPC capture and maintain genetic and phenotypic heterogeneity. (A) Serial sections of tumor biopsy tissue stained with hematoxylin and eosin (H&E) or the indicated antibodies. Magnified views of Region-1 (R1) and Region-2 (R2) are shown. Scale bars, 50 μ M. (B) Patient biopsy-derived organoid sections stained with H&E or the indicated antibodies. Scale bars, 200 μ M. (C) Phylogenetic tree of primary tumor and metastasis-derived organoids. Primary prostate tumor, 1^o. PC35-1 subclones—35-1a and 35-1b. PC35-2 subclones—35-2a and 35-2b. Significant genetic events are indicated at positions in the tree where they originated. (D) PC35-1 organoids were dissociated into single cells and stained by immunofluorescence (IF) with antibodies against the indicated proteins and DAPI. Each of 4 phenotypes is indicated by a number and arrow. 1 = AR^{POS}/CHGA^{Lo/NEG}; 2 = AR^{NEG}/CHGA^{Hi}; 3 = AR^{POS}/CHGA^{Hi}; 4 = AR^{NEG}/CHGA^{Lo/NEG}. (E) The Weill Cornell Medicine cohort of mCRPC (black filled circles) and the indicated models used in this study are plotted by AR signaling score and NEPC score. (F) Continuous EdU-incorporation assay for the indicated organoid lines. The graph shows the percentage of EdU-positive cells over time. Dashed lines mark the approximate day of population doubling for each. Bar and line graphs are plotted as the mean of 3 independent experiments. Error bars represent \pm SEM.

To validate the scRNAseq analysis and to develop a quantitative assay for specific subpopulations, we performed quantitative single-molecule RNA-FISH using selected markers on PC35-1/2 organoid-derived cells (Supplementary Figure S6). In agreement with the scRNAseq results, we found ARPC lineage marker-positive cells, NEPC marker-positive cells, and double-positive cells (Supplementary Figure S6A). EZH2 and TK1 marked the same population of EdU-positive, dividing cells (Supplementary Figure S6A-S6C). Double staining for mRNA and protein of selected lineage markers confirmed a strong positive correlation between mRNA and protein (Supplementary Figure S6D).

Simultaneous tracking of lineage and clonal identity with single-cell resolution identifies self-renewing stem-like subpopulations with differentiation potential

To address the dynamic plasticity and the hierarchical structure of the subpopulations, we used the “CellTagging” method of combinatorial indexing of expressed barcodes, determined by scRNAseq, to simultaneously track cellular origin and phenotypic identity within growing organoids.²¹ We analyzed single time point experiments of different durations after tagging to identify the clonal expansion of sibling cells, allowing determination of the clonal relationships for lineage-marked

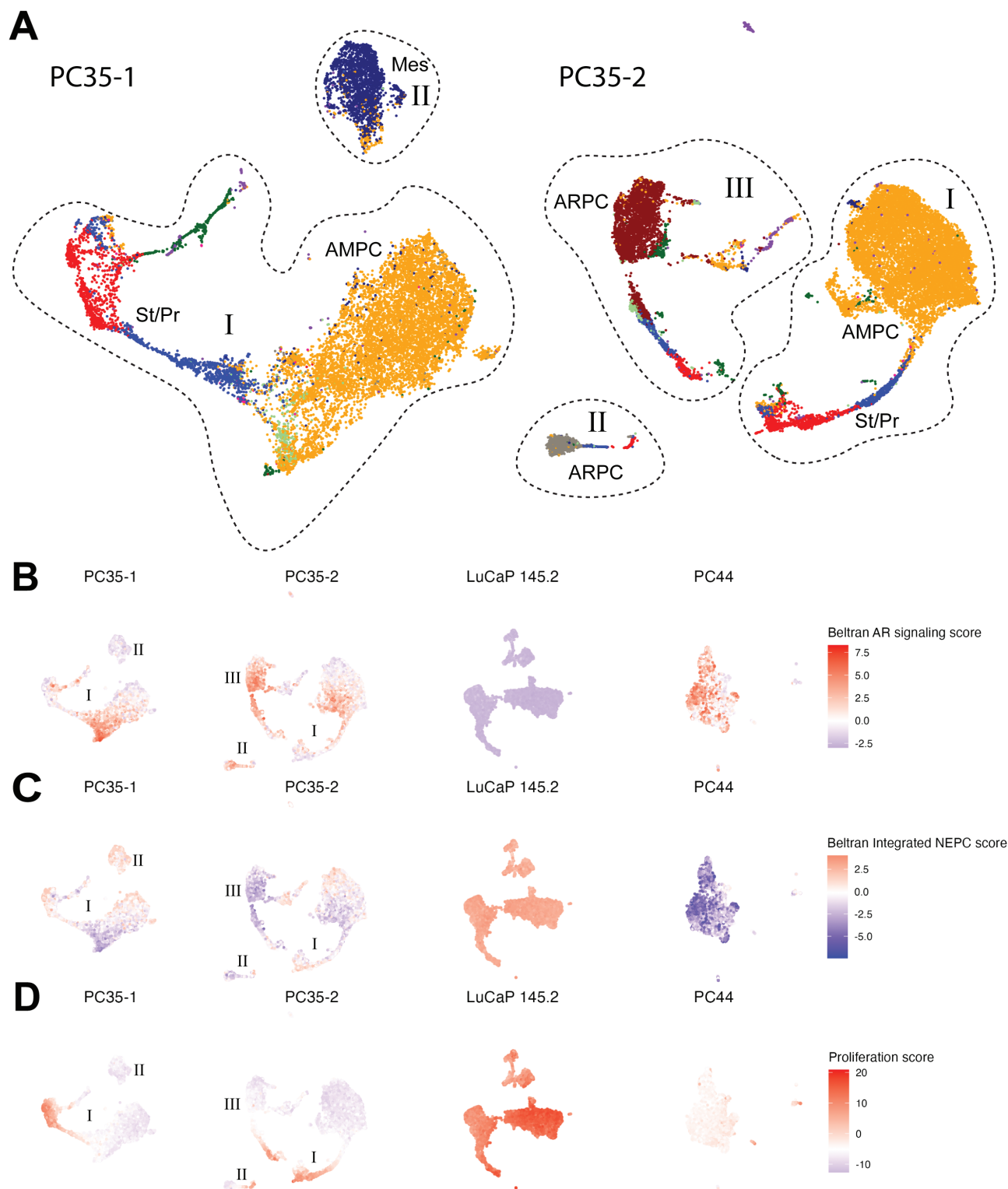


Figure 2. Single-cell transcriptomics identifies lineage-distinct heterogeneity in the PC35 organoid models (A) scRNAseq transcriptomic profiles of PC35-1 and PC35-2 organoids plotted as UMAPs. Major clusters are circled and labeled with Roman numerals. Clusters are colorized by phenotype designations, which are further characterized in Figure 4 and Supplementary Figure S9. Broad designations include stem/progenitor (St/Pr) = red and blue, adenocarcinoma (ARPC) = brown (NR3C1-enriched) and gray, amphicrine (AMPC) = orange, or mesenchymal (Mes) = dark blue. (B) AR and (C) neuroendocrine (NE) signature scores for each cell determined by principal component analysis (PCA) using published gene sets from Beltran et al. Loadings from the first principal component for each cell are projected onto the UMAPs from (A) and UMAPs plotted for LuCaP 145.2 and PC44 scRNAseq transcriptomic data. (D) Proliferation score was determined as in (B) and (C) using a proliferation gene set derived from Balanis et al.

populations. A separation of 4 weeks between tagging and harvest captured uniquely tagged clones in all major clusters. For both PC35-1 and PC35-2, all tagged clonal sibling cells that were associated with any given major cluster were exclusive to that cluster, demonstrating the clonality of each cluster. The location of tagged sibling cells is graphically depicted on the UMAPs for PC35-1/2 with black lines connecting clones (Figure 3A, 3B). Within each major cluster, a disproportionate number of the tagged clones were located entirely within the St/Pr subclusters (quantified in Supplementary Figure S7), indicating self-renewal. Tagged St/Pr clones also spanned across the differentiated subclusters within the same major cluster, demonstrating differentiation. The more differentiated subclusters showed very limited internal cellular replication, suggesting that differentiation from a cancer St/Pr cell was the major source of amphoteric cells.

In contrast, the clones captured in LuCaP 145.2 NEPC organoids were indicative of a widely proliferative population. We detected numerous clones both within and nondirectionally across the 2 major phenotypically identified stem cell (SC) populations, while the more differentiated NE population (colored purple) contained no tagged clones (Figure 3C). The ARPC model PC44 exhibited 2 phenotypes of dividing cells, a high number of clones associated with 2 small clusters and giving rise to differentiated daughters as well as self-renewing cells within the main luminal cluster (Figure 3D). In contrast, AR⁺ cells derive mainly from SCs in the AMPC model.

One possible explanation for the discrete clonality of the major clusters in the PC35 models is that cluster-specific genetic events led to distinct phenotypes, although we were unable to identify subclonal driver mutations by WGS analyses. We analyzed our scRNAseq data using CopyKAT to identify clonal subpopulations based on genomic copy number variation (CNV) and associated this genomic substructure with the phenotypically defined major clusters.²² We found 2 patterns defined by contributing CNV-identified clones to the different phenotypes of the clusters: those which were independent of clonal patterns (AMPC, mesenchymal, and PC35-1 ARPC clone II phenotypes) and those attributed to unique or closely related clonal genotypes (the PC35-2 ARPC III clone; Figure 3E; Supplementary Figure S8A, S8B). These data suggest that there are fixed differentiation patterns for preexisting clonal populations in addition to common pathways of lineage plasticity, demonstrating genetically determined (clonal) and inherent differentiation pathways contributing to phenotypic heterogeneity.

Integration of scRNAseq across CRPC models suggests distinct growth patterns associated with lineage subtypes

To compare tumor subpopulations among ARPC, AMPC, and NEPC, we integrated scRNAseq data across the organoid models and, in addition, included published scRNAseq data from 2 commonly used metastatic cell lines, LNCaP and VCaP (Figure 4A, 4B). We also mapped individual, tagged daughter cells onto the integrated clusters (Figure 4C). The distribution of clusters among the models and their relative expression of AR, NE, MYC, and St/Pr signatures is shown (Figure 4C). Additional lineage and relevant biological signature enrichments are shown in Supplementary Figure S9.

All models contained St/Pr cell populations, which separated into 2 subclusters. St/Pr 1 (colored red) appeared

to be the originating stem population, while St/Pr-2 (colored blue) demonstrated transcriptomic properties of a transit-amplifying subpopulation, as well as defining the cluster proximal in similarity to differentiated cells. Of interest, we queried for a variety of developmentally identified luminal SC markers including KRT13, LY6D, CD133, and PSCA.²³ The 3 former markers were not expressed in the models investigated here. PSCA was expressed across most of the clusters in the PC44 adenocarcinoma model, consistent with a luminal lineage marker. While the St/Pr populations were relatively minor in the ARPC and AMPC models, they composed the majority of the scNEPC cells (Figure 4B).

The St/Pr signature overlaps with a signature termed “Persist,” which was identified in LNCaP cells from a subpopulation resistant to the AR antagonist enzalutamide, and computational approaches inferred “Persist” as a founding trajectory population.²⁴ Similarly, in primary prostate cancers, the “Sig51” signature, which was shown to correlate with increased aggressiveness, overlaps the integrated St/Pr signature (Supplementary Figure S9).²⁵ By contrast, the gene set defining the recently described, mesenchymal stem-like PC subpopulation (termed MSPC) in bulk cultures of mCRPC cell lines, organoids, and xenografts²⁶ was not substantially enriched in the St/Pr signature defined here. In addition, using experimental lineage tracing, we show here for the first time in CRPC models a direct one-to-one correspondence in individual cells between either self-renewal or the generation of differentiated daughter cells and the expression of a gene signature (St/Pr), which has been associated with enzalutamide resistance and clinical aggressiveness.

The ARPC cell line models share a major population (cluster 5, enriched for genes found in mouse basal and castration-resistant luminal cells), which is a minor population in the organoid models (Figure 4A, 4B). However, in the organoid models, cluster 5 cells are juxtaposed or intermixed with St/Pr-2 cells, and in some cases, demonstrate evidence of division using lineage tracing (Supplementary Figure S7). One possibility is that cluster 5 cells represent an intermediary cell that may have been expanded in the continuous growth of cell lines selected on a 2 dimensional surface.

Amphoteric cell populations, which have yet to be thoroughly characterized due to their rarity in tractable models, are found in the NCI-PC351/2 and the VCaP cell line (Figure 4A, 4B). Signatures characterizing amphoteric populations (clusters 3, 7, 8, and 10) include senescence, mesenchymal, “Progenesis” (regenerative luminal cells enriched for basal and mesenchymal features),²⁷ MSPC,²⁶ and clusters from LNCaP models that have been selected by long-term growth in enzalutamide (Supplementary Figure S9).²⁴ This suggests that amphoteric transcriptomes are a component of various cell lines and mouse models describing progression following AR signaling suppression of ARPC.

Single-cell ATACseq reveals TFs regulating amphoteric SC, luminal, and mesenchymal pathways

As the transcriptional determinants of the amphoteric lineage are largely unknown, we performed single-cell assay for transposase accessible chromatin (ATAC)seq on PC35-1/2 organoids. Clustering by genome-wide chromatin accessibility yielded 3 clusters¹⁻³ in both PC35-1 and PC35-2 (Figure 5A). To look for TFs that may be responsible for the

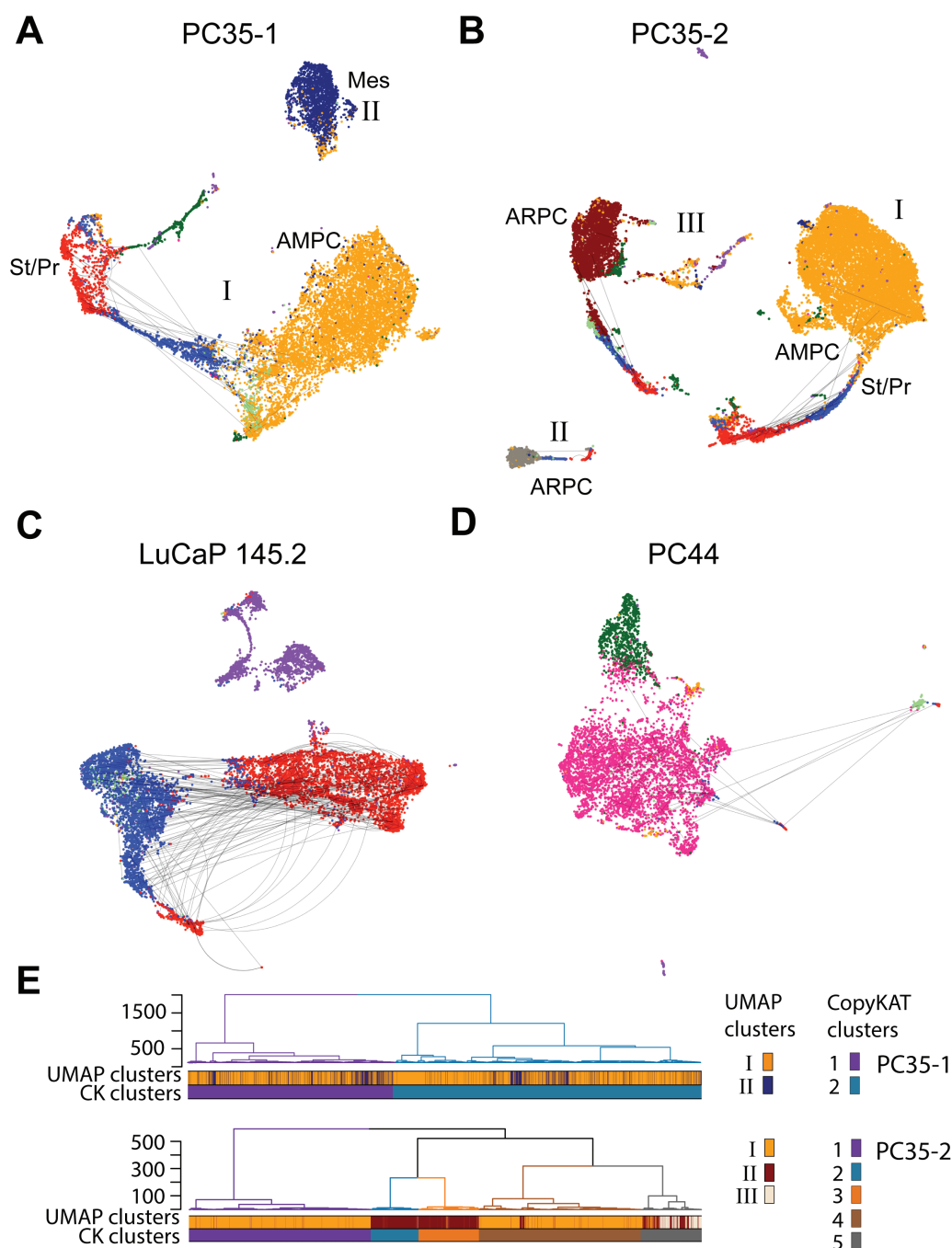


Figure 3. Single-cell combinatorial barcoding identifies lineage-distinct and stem-like/progenitor subpopulations (A-D) CellTag lineage tracing analysis. Clusters are colored by phenotypes further defined in Figure 4 and Supplementary Figure S9. (A) UMAP major clusters I and II of PC35-1 and (B) I, II, and III of PC35-2 are shown. Each cell in a clonal population (≥ 2 cells expressing the same combination of barcode IDs), is connected by a black line. Self-renewing clones that exist in the same subcluster are connected by curved lines, differentiating clones that span at least 2 subclusters are connected by straight lines. (C) Clonal connections as in (A) and (B) mapped onto (C) LuCaP 145.2 and (D) PC44 UMAPs. (E) Comparison of subpopulations defined by their scRNAseq transcriptional profile (UMAP clusters), to subclones defined by genomic CNV (CopyKAT clusters) determined using the same scRNAseq data. Results for both PC35-1 (top) and PC35-2 (bottom) are shown. Dendrograms are colored according to CopyKAT cluster number and show the hierarchical relationships among the CopyKAT clusters. Heatmaps directly below the dendrograms show the distribution of cells from UMAP major clusters I, II, and III throughout the CopyKAT clusters. Each cell is represented by a vertical line colored according to the UMAP cluster (top row) or the CopyKAT cluster (bottom row) to which it belongs and sorted by CopyKAT cluster. PC35-2 contains 2 additional minor UMAP clusters lacking differentially expressed genes that were not annotated here.

differing phenotypes among the clusters, we performed an analysis of inferred TF activity and assessed the similarity with ATACseq-based signatures describing various subclasses of clinical mCRPC or dynamic states of lineage transition^{26,28} (Figure 5B-5D).

Cluster 3 in both models were distinguished as mesenchymal and lacking SC, ARPC, NEPC, and WNT-driven phenotypes (Figure 5D). These clusters were notable for a relative absence of REST activity and high activity scores for TFs such as NRF1, HES4, and ONECUT2 (Figure 5B, 5C).

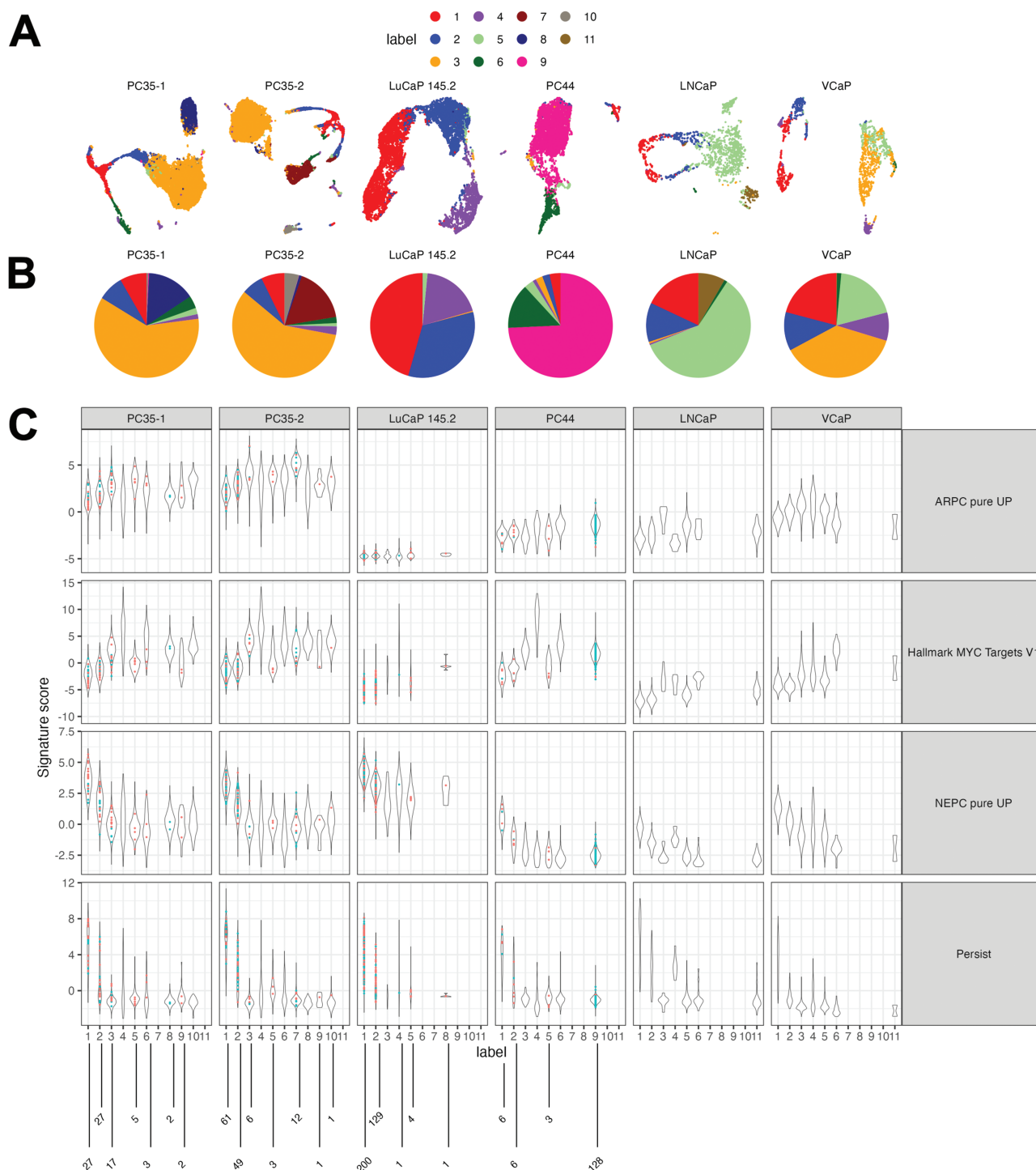


Figure 4. Integration of organoid cohort with LNCaP and VCaP cell lines shows common phenotypes across samples. (A) UMAP embeddings of integrated scRNAseq for NCI-PC35-1/2, LuCaP145.2, and NCI-PC44 organoid cultures and LNCaP and VCaP cell lines using mutual nearest neighbors correction. Each UMAP was generated using the batch corrected principal components for each sample independently. Cells are colored based on clustering membership using integrated data for all samples. 1) Stem/progenitor (St/Pr)-1, 2) St/Pr-2, 3) AMPC, 4) NEPC, 5) ARPC/luminal stem,²⁷ 6) ARPC/NR3C1^{HI}, 7) AMPC, 8) mesenchymal, 9) ARPC/NR3C1^{HI}, 10) AMPC, 11) ARPC/luminal stem, (B) Pie charts show the relative proportion for each cluster in each sample. (C) Violin plots show signature scores relative to cluster and model. Colored dots are signature scores for individual cells that were determined to be CellTagged clones. Red dots are self-renewing clones, blue dots are differentiating clones. The number of clones is enumerated below each cluster.

Clusters 1 and 2 in PC35-1/2 demonstrated unique but highly overlapping combinations of TFs contributing to SC, luminal epithelial, and neural phenotypes. Additionally, clusters 1 and 2 of both models could be partitioned into 2 pairs of subclusters 1.1, 1.2, and 2.1, 2.2 (Figure 5B). Inferred

TF activities in subclusters 1.1 and 2.1 were consistent with a stem-like phenotype, while 1.1 and 2.1 were enriched for ATAC signatures determining luminal epithelial and transitional mesenchymal lineages, respectively (Figure 5D). The “transition” signature includes JAK/STAT inflammatory

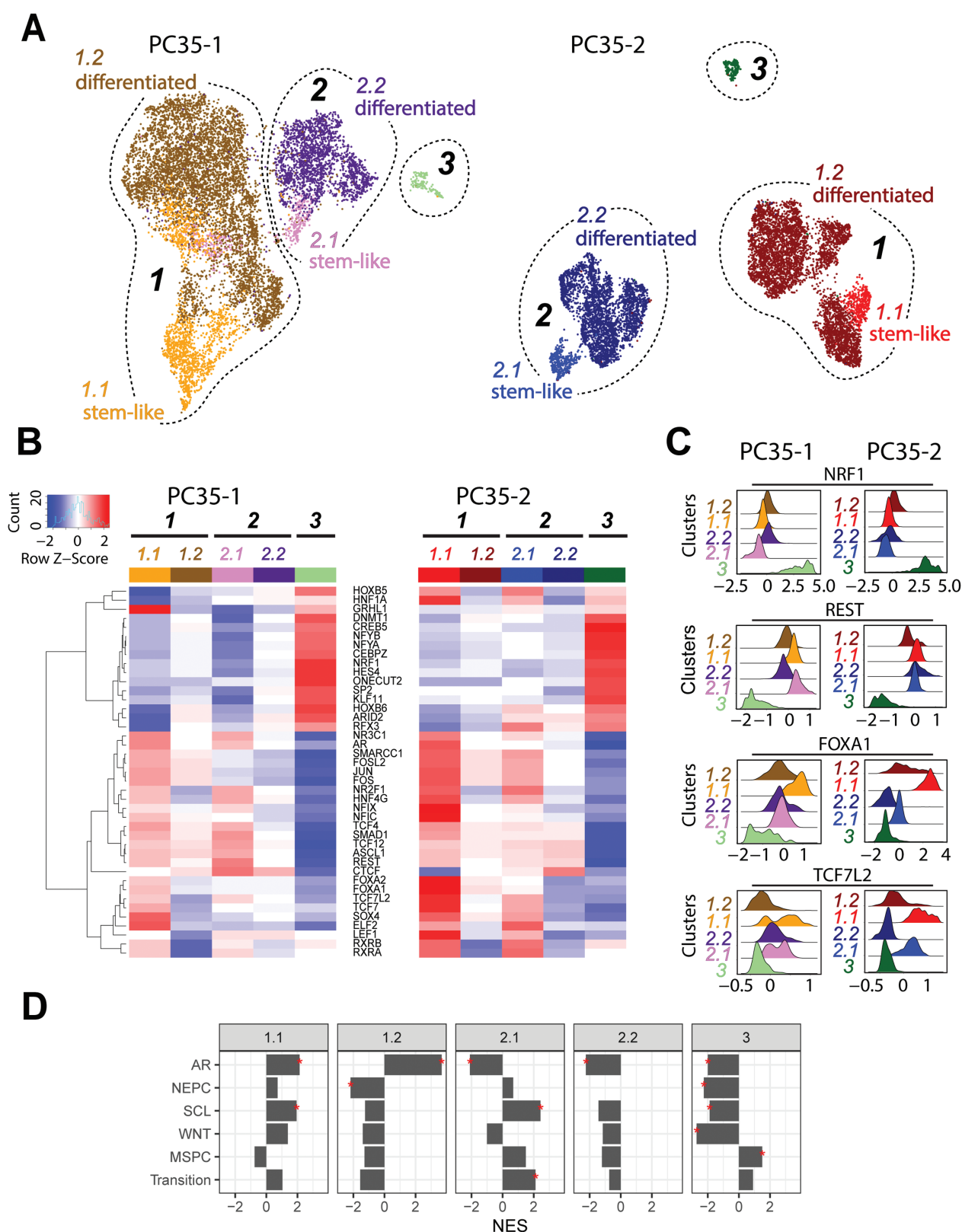


Figure 5. scATACseq clusters NEPC and ARPC populations in the PC35 organoids (A) UMAPs of global chromatin accessibility for PC35-1 and PC35-2. Major clusters are annotated as 1, 2, 3. Clusters 1 and 2 are partitioned into 2 additional subclusters, stem-like and differentiated. (B) Heatmaps show inferred transcription factor (TF) activities of the listed TFs for each of the UMAP clusters/subclusters in PC35-1 and PC35-2. The heatmaps are colored by deviations z-scores, calculated as the differential accessibility for a particular TF compared to the average accessibility profile for the entire dataset. TF activity shown was selected using the score markers function (see [Supplementary Methods](#)) on the deviations z-scores to identify maximal enrichment across lineages and development. TFs shown were determined to be expressed and selected from a list of the top 50 most deviant TFs. (C) Inferred TF activity density plots for each cluster population. Deviations z-scores are shown on the x-axis for the TF indicated at the top. Density estimates are represented along the y-axis and broken down by cluster/subcluster. (D) Normalized enrichment scores derived using GSEA for each cluster across molecular phenotyping signatures. Significant scores are denoted with "*" (adjusted $P \leq 0.05$).

processes, which bridges SC and neural populations in a dynamic mouse model.²⁹ Consistent with the expression of NE markers in a mouse model transitioning from adenocarcinoma to NEPC, ASCL1, and FOXA2 TF activities were observed, but other classical scNEPC TFs such as MYCN, BRN2, or NEUROD1 were not apparent.³⁰⁻³² Of interest, a WNT-related signature was exclusively expressed in the luminal epithelial SCs but lost in the transitional mesenchymal population. These data extend and contextualize previously defined CRPC subclass signatures to plasticity-mediated subpopulations.

There were no remarkable TF activities gained in clusters 1.2 and 2.2 compared to the stemlike 1.1 and 2.1. The defining signatures in 1.2 were enriched AR-driven and depleted NE signatures, while 2.2 demonstrated a depleted AR signature. Of interest, differentiation was mostly associated with reduced TF activity relative to the stem-like clusters. One possible explanation for this is that the plasticity-associated heterogeneity across the differentiating population obscured TF patterns. This is supported by the observation that there is a loss of accessibility for the TFs shown in Figure 5B, while the average global number of accessible sites did not change. These data suggest a model of plasticity whereby the activity of a transitional mesenchymal lineage program on luminal stem-like/progenitor clones resulted in distinct cellular phenotypes that share to differing degrees features of ARPC and NEPC lineages, as observed in the major amphicrine cellular population.

Targeting both AR pathway-dependent and independent compartments of the St/Pr subpopulations inhibits in vitro and in vivo tumor growth

The existence of multiple identifiable clones propagated almost exclusively by St/Pr cells in the AMPC model implies an approach to treatment. Because at least a portion of the St/Pr population expressed AR, we incubated PC35-1 and PC35-2 organoids with enzalutamide, quantified cell numbers, and found a partial response in both models, concordant with the notion of a subpopulation-specific dependence on AR signaling (Supplementary Figure S10A). PC35-1 showed a greater than 2-fold reduction after treatment, while PC35-2 showed a less than 30% decrease. We then performed RNA-FISH in combination with EdU to quantify subpopulation-specific changes due to enzalutamide treatment (Supplementary Figure S10B-S10D). Congruent with the different overall response observed in bulk, we found that enzalutamide caused a >10-fold reduction to proliferating AR^{POS}EdU^{POS} cells in PC35-1, while the same population in PC35-2 showed only a small decrease (Supplementary Figure S10C). PC35-2 demonstrates an NR3C1-dependent signature, consistent with enzalutamide resistance (PC35-2 cluster 7, Supplementary Figure S9). The SCG2-positive, NE-like, populations in both PC35-1/2 were insensitive to enzalutamide (Supplementary Figure S10D).³³ These data document treatment-resistant variability selected within a single patient tumor consisting of distinct clonal lineages.

Although AR^{POS} cells made up a proportion of the EdU^{POS} progenitor population, ≥50% of St/Pr cells were AR negative (Supplementary Figure S10C, -Enza columns). To specifically address the St/Pr population, we identified multiple druggable targets as highly enriched in the St/Pr clusters, including EZH2, AURKA, and the Notch pathway (Supplementary

Figure S4B, S4C) and targeted them with CPI-1205, alisertib, or Compound E, (EZH2i, AURKAi, and Notchi, respectively). For comparison, we included the chemotherapeutic agent carboplatin, which is used as a late line of therapy in mCRPC. We treated the PC35 organoids with AURKAi, EZH2i, Notchi, carboplatin, or DMSO for 6 weeks. In both organoid models, the AURKAi caused a nearly 10-fold decrease in cell number compared to DMSO while the other drug conditions resulted in only minor reductions (Figure 6A). We tracked the effect of AURKAi, EZH2i, and carboplatin relative to DMSO with single-cell resolution using RNA-FISH/EdU combined assays. Subpopulations were identified by marker gene expression: AR to mark ARPC lineage; SCG2 to mark NEPC lineage; TK1, EZH2, and AURKA to mark stem-like/progenitors. We found that the AURKAi specifically depleted the dividing, EdU-incorporating stem-like/progenitor subpopulation in PC35-1/2 (Figure 6A, 6B), while the SCG2 population increased as a percentage of the total (Figure 6B, 6C). By comparison to AURKA inhibition, carboplatin treatment of PC35-1/2 had no effect (Figure 6A-6C).

To evaluate how effective inhibition of AURKA and/or AR is at blocking tumor growth in vivo, we treated PC35-1 organoid-derived xenograft tumors for 9 weeks with either alisertib, castration, alisertib combined with castration, or vehicle. Castration or alisertib (30 mg/kg once/day) alone caused a 50% decrease in tumor growth. However, the combination treatment rapidly and dramatically blocked tumor growth (Figure 6D). In addition, an alternative dose schedule of alisertib (20 mg/kg twice/day) alone, designed to maintain a continuous efficacious exposure level, caused tumor regression (Figure 6E). We validated the loss of dividing cells and retention of differentiated amphicrine cells in the residual tumor bed (Supplementary Figure S11). In 9-week CT35 tumors, castration caused a strong increase in cytoplasmic and decrease in nuclear AR, as well as increased expression of the NE marker, synaptophysin (Supplementary Figure S11A). Consistent with the effects on tumor growth, the strong BrdU incorporation observed in the control was decreased in all the treated conditions, reaching the lowest level in the combination treatment (Supplementary Figure S11A, S11B). These results demonstrate that the subpopulation-specific vulnerabilities that we identified in patient-derived organoids can be exploited to yield impactful results on tumor growth in vivo.

Discussion

There is a growing appreciation for the role of lineage plasticity in drug resistance and progression. Amphicrine (AR⁺NE⁺) CRPC tumors are thought to be an early indicator of lineage plasticity and are of particular interest in providing models to investigate mechanisms associated with lineage losses and gains. The amphicrine model investigated here and characterized by mutations in the epigenetic regulators, *ARID1A* and *ARID1B*, and the cell cycle regulator, *CDKN1B*, exhibited at the single-cell level all permutations of luminal epithelial and NE lineage marker expression. Although clinical amphicrine CRPC has been characterized for pathological and molecular features, tractable cell models have been limited to the VCaP cell line. Integrating scRNAseq data across multiple models and applying various CRPC lineage signatures revealed that amphicrine populations were enriched for mesenchymal SC, regenerative, and enzalutamide

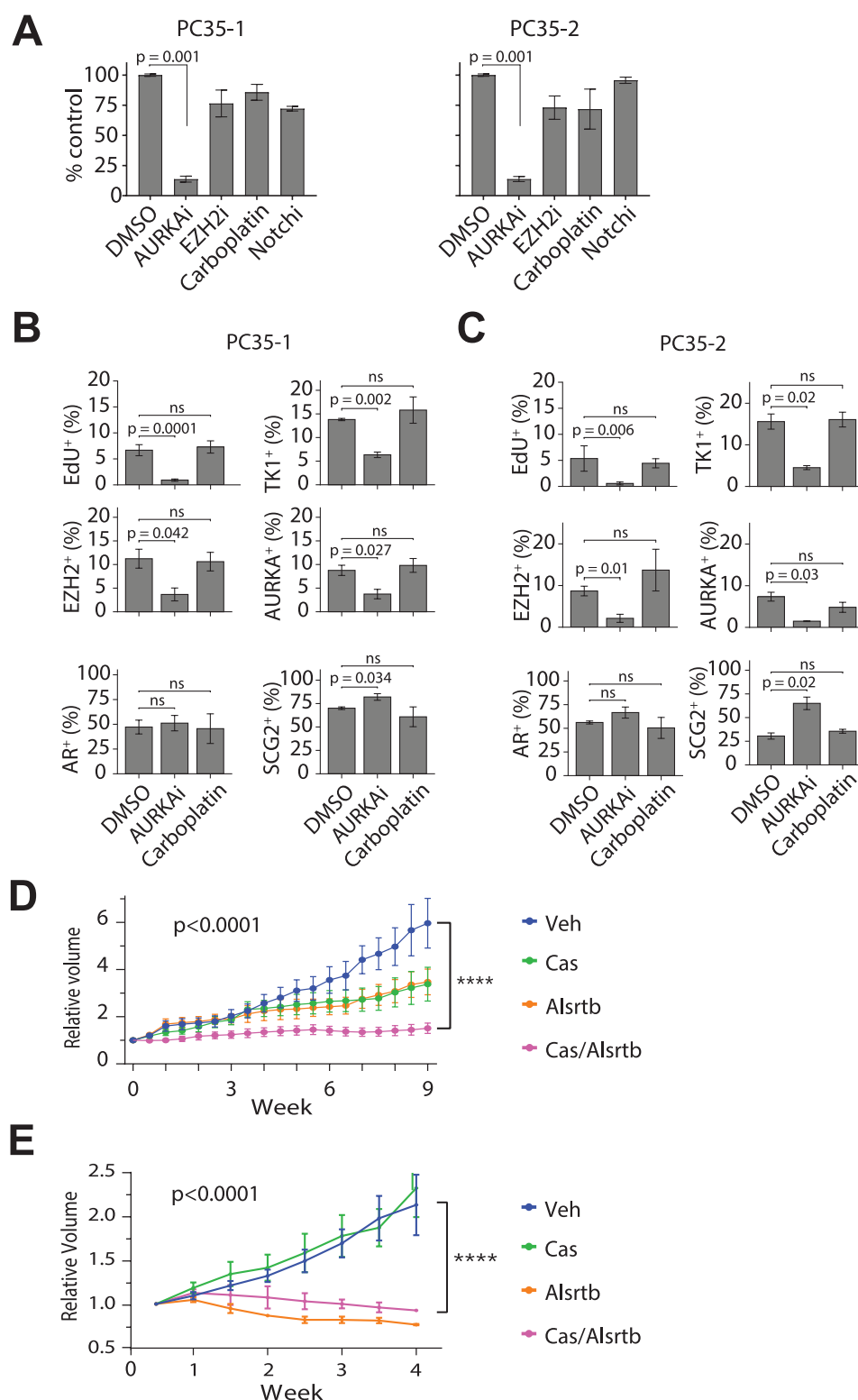


Figure 6. The stem-like/progenitor subpopulation is vulnerable to AURKA inhibition (A) Determination of drug sensitivity. Organoids were treated twice weekly for 6 weeks with 500 nM AURKai, 500 nM EZH2i, 500 nM carboplatin, 1 μ M Notchi, or 0.02% DMSO-treated controls. Quantification was done by dissociating the organoids and manually counting the cells. The quantified values for each condition were plotted relative to the DMSO controls. (B) PC35-1 and (C) PC35-2 organoids treated for 6 weeks as in (A) with AURKai, carboplatin, or DMSO, then pulsed with 10 μ M EdU, 24 hours prior to collection. The indicated marker expression for each cell was determined by RNA-FISH. EdU-incorporation status (positive or negative) was determined for each cell. Data was plotted as the percentage of cells that were positive for a given marker or EdU for the 3 treatment conditions. (D&E) Relative change in tumor volume for PC35-1 organoid-derived xenografts (ODXs). Mice were dosed with alisertib (Alisertb) 30 mg/kg once-daily for 9 weeks (D) or with 20 mg/kg twice-daily for 4 weeks (E) or vehicle (Veh) (D&E). Tumor volume was calculated as an average of the replicates. The change in volume was calculated relative to the "0" time point (~150 mm³ tumor volume). Vehicle $n = 5$ mice; castration $n = 5$ mice; alisertib $n = 4$ mice; castration + alisertib $n = 5$ mice. Error bars, \pm SEM. P -values were calculated using the Student's t test, 2-tailed, unpaired.

resistance characteristics, which are often linked with prostate cancer progression.^{24,27,29}

We show the existence of clonally distinct cancer St/Pr subpopulations as the source of growth and phenotypic heterogeneity. Defining the relationship of CRPC SCs to developmentally identified, castration-resistant prostate luminal SCs remains an important question.²³ Surprisingly, the least proliferative population was the most NE-like. This finding is contrary to the increased growth rate of AR⁻ NEPC driven by *RB1* and *TP53* loss, but consistent with less aggressive NE tumors including gastroenteropancreatic NE neoplasms, breast cancer with NE differentiation, and pulmonary NE carcinoids that are frequently driven by mutations in *ARID1A*.¹⁴⁻¹⁶ This model is evidence for the concept that SC plasticity per se does not correlate with aggressiveness but that additional drivers are needed to overcome proliferative arrest associated with terminal differentiation. To the best of our knowledge, this is the first near-patient CRPC organoid that dynamically produces a range of phenotypically heterogeneous daughters. Additional models of amphicrine CRPC are needed to obtain a more complete understanding of the range of biological characteristics.

Diversified and labile transcriptional programs within a heterogeneous tumor cell population can rapidly confer clonal fitness in the face of therapeutic pressure.^{24,34-36} In addition to lineage switching, we found ARPI resistance in independent clones mediated by other potential mechanisms, such as high expression of *NR3C1*. This observation directly demonstrates within a patient CRPC tumor that multiple different paths to AR resistance exist within the same tumor, underscoring the challenges in the development of curative treatments.

Despite the range of lineage heterogeneity, scATACseq identified 2 major populations of amphicrine SCs with overlapping inferred TF activity. Two populations were distinguished by ATAC signatures representing respectively either ARPC and WNT pathway or transitional JAK/STAT and mesenchymal pathways. The latter signature is kinetically associated with cells in a GEMM model that bridge adenocarcinoma and NE population transitions,²⁹ suggesting a contribution in PC35 amphicrine cells to the expression of NE markers such as *CHGB*. Of interest, the differentiated populations had equally accessible global chromatin relative to the SC state but reduced inferred activity for a variety of the TFs. One interpretation of this data is that plasticity is associated with a widely accessible chromatin state followed by heterogeneous and perhaps stochastic chromatin closing during commitment.

The existence of a stem-like/progenitor subpopulation as the seedbed of growth in a tumor predicts excellent potential as a point at which to direct therapeutic intervention. We found Aurora Kinase A, a regulator of mitotic progression, SC self-renewal, and asymmetric division,^{22,37,38} to be expressed and restricted to the St/Pr. Interestingly, in a mouse model of incisor development, *ARID1A* was shown to be a transcriptional repressor of *Aurka*, while loss of *ARID1A* led to *AURKA* overexpression and expanded transit-amplifying cells with abnormal differentiation.³⁹ Inhibition of *AURKA* in the organoid models caused a strong and specific depletion of the St/Pr pool that blocked the growth of the entire heterogeneous population and importantly, blocked tumor growth in vivo. Using lineage tracing in combination with scRNAseq, we observed in the PC44 ARPC model, the existence of 2 pools of dividing tumor cells, a minor St/Pr population, and

a self-renewing luminal epithelial population. Thus, we anticipate that alisertib alone would likely not be useful in most ARPC tumors but may be beneficial in combination with AR pathway inhibitors to suppress the dividing St/Pr population that is insensitive to AR inhibition.

Clinical trials targeting the treatment of scNEPC with alisertib have been mostly ineffective. Our analysis of the population structure and its relationship to cell division potentially provides insight >70% of the scNEPC cells had a St/Pr phenotype. Besides the underlying physiological differences attributable to distinct genomic mutations in scNEPC such as *RB1* loss, it is expected that targeting a major as compared to a minor population of St/Pr tumor cells would increase the probability of resistance. In total, the results presented here establish the utility of alisertib for a cancer SC-driven model of AMPC and suggest that alisertib be tested as a combination agent for ARPC to assist with the development of lineage plasticity-mediated resistance to AR pathway inhibitors.

Acknowledgments

We wish to express our gratitude to the patients and the families of the patients who contributed to this study. We would like to thank the LGCP Microscopy Core at the NCI/CCR and we would like to thank the CCR Single-cell Analysis Facility. Sequencing was performed with the CCR Genomics Core. This work used the computational resources of the NIH HPC Biowulf cluster (<http://hpc.nih.gov>). We would like to thank A. Zoubeydi for providing the EZH2 phospho-T350 antibody. We thank D. Takeda, G. Merlino, J. Shern, and M. Shen for reviewing the manuscript.

Author contributions

Conceptualization: Michael L. Beshiri, Kathleen Kelly. Methodology: Michael L. Beshiri, Samantha A. Morris, Supreet Agarwal, Fatima H. Karzai, William L. Dahut, Kathleen Kelly. Investigation: Michael L. Beshiri, Ross Lake, Adam G. Sowalsky, Danielle Burner, Caitlin M. Tice, Crystal Tran, Julianna Kostas, JuanJuan Yin, Aian Neil Alilin. Formal analysis: Michael L. Beshiri, Brian J. Capaldo, Anson T. Ku, Kathleen Kelly, Ross Lake, Adam G. Sowalsky, JuanJuan Yin, Tamara L. Lotan. Visualization: Michael L. Beshiri, Brian J. Capaldo, Ross Lake, Anson T. Ku. Project administration: Michael L. Beshiri, Kathleen Kelly. Supervision: Kathleen Kelly. Writing: Michael L. Beshiri, Kathleen Kelly.

Funding

This research was supported by the Intramural Research Program of the NIH, National Cancer

Institute, Center for Cancer Research; Prostate Cancer Foundation (Young Investigator Awards to M.L.B. and A.G.S.); Department of Defense Prostate Cancer Research Program (W81XWH-16-1-0433 to A.G.S.); and support from CCR Single Cell Analysis Facility was funded by FNLCR Contract (HHSN261200800001E).

Conflicts of interest

S.A.M. declared employment at Washington University in St Louis and co-founder of CappyBio Inc. T.L.L. declared research funding from AIRAMatrix, DeepBio, Exact Biosciences.

A.G.S. declared research funding from Astellas (via CRADA). The other authors declared no potential conflicts of interest.

Data availability

The sequence information for all RNA-FISH probe sets is located in [Supplementary Table S1](#). The WGS, scRNAseq, and scATACseq data underlying this article have been deposited in Database of Genotypes and Phenotypes (dbGaP) and Gene Expression Omnibus (GEO) at <https://www.ncbi.nlm.nih.gov/gap/> and <https://www.ncbi.nlm.nih.gov/geo/>, respectively, and can be accessed with phs001587.v2.p1 (dbGaP) and GSE237603 (GEO).

Supplementary material

Supplementary material is available at *Stem Cells* online.

References

- Quintanal-Villalonga A, Chan JM, Yu HA, et al. Lineage plasticity in cancer: a shared pathway of therapeutic resistance. *Nat Rev Clin Oncol*. 2020;17(6):360-371. <https://doi.org/10.1038/s41571-020-0340-z>
- Beltran H, Prandi D, Mosquera JM, et al. Divergent clonal evolution of castration-resistant neuroendocrine prostate cancer. *Nat Med*. 2016;22(3):298-305. <https://doi.org/10.1038/nm.4045>
- Mu P, Zhang Z, Benelli M, et al. SOX2 promotes lineage plasticity and antiandrogen resistance in TP53- and RB1-deficient prostate cancer. *Science*. 2017;355(6320):84-88.
- Balanis NG, Sheu KM, Eshed FN, et al. Pan-cancer convergence to a small-cell neuroendocrine phenotype that shares susceptibilities with hematological malignancies. *Cancer Cell*. 2019;36(1):17-34.e7. <https://doi.org/10.1016/j.ccell.2019.06.005>
- Aggarwal R, Huang J, Alumkal JJ, et al. Clinical and genomic characterization of treatment-emergent small-cell neuroendocrine prostate cancer: a multi-institutional prospective study. *J Clin Oncol*. 2018;36(24):2492-2503.
- Bluemn EG, Coleman IM, Lucas JM, et al. Androgen receptor pathway-independent prostate cancer is sustained through FGF signaling. *Cancer Cell*. 2017;32(4):474-489.e6. <https://doi.org/10.1016/j.ccell.2017.09.003>
- Labrecque MP, Coleman IM, Brown LG, et al. Molecular profiling stratifies diverse phenotypes of treatment-refractory metastatic castration-resistant prostate cancer. *J Clin Invest*. 2019;129(10):4492-4505. <https://doi.org/10.1172/JCI128212>
- Beshiri M, Agarwal S, Yin JJ, Kelly K. Prostate organoids: emerging experimental tools for translational research. *J Clin Invest*. 2023;133(10):1-6.
- Kadoch C, Hargreaves DC, Hodges C, et al. Proteomic and bioinformatic analysis of mammalian SWI/SNF complexes identifies extensive roles in human malignancy. *Nat Genet*. 2013;45(6):592-601. <https://doi.org/10.1038/ng.2628>
- Centore RC, Sandoval GJ, Soares LMM, Kadoch C, Chan HM. Mammalian SWI/SNF chromatin remodeling complexes: emerging mechanisms and therapeutic strategies. *Trends Genet*. 2020;36(12):936-950. <https://doi.org/10.1016/j.tig.2020.07.011>
- Sun X, Chuang JC, Kanchwala M, et al. Suppression of the SWI/SNF component *arid1a* promotes mammalian regeneration. *Cell Stem Cell*. 2016;18(4):456-466. <https://doi.org/10.1016/j.stem.2016.03.001>
- Nagarajan S, Rao SV, Sutton J, et al. ARID1A influences HDAC1/BRD4 activity, intrinsic proliferative capacity and breast cancer treatment response. *Nat Genet*. 2020;52(2):187-197. <https://doi.org/10.1038/s41588-019-0541-5>
- Xu G, Chhangawala S, Cocco E, et al. ARID1A determines luminal identity and therapeutic response in estrogen-receptor-positive breast cancer. *Nat Genet*. 2020;52(2):198-207. <https://doi.org/10.1038/s41588-019-0554-0>
- Marchio C, Geyer FC, Ng CK, et al. The genetic landscape of breast carcinomas with neuroendocrine differentiation. *J Pathol*. 2017;241(3):405-419. <https://doi.org/10.1002/path.4837>
- Cros J, Théou-Anton N, Gounant V, et al. Specific genomic alterations in high-grade pulmonary neuroendocrine tumours with carcinoid morphology. *Neuroendocrinology*. 2021;111(1-2):158-169. <https://doi.org/10.1159/000506292>
- Puccini A, Poorman K, Salem ME, et al. Comprehensive genomic profiling of gastroenteropancreatic neuroendocrine neoplasms (GEP-NENs). *Clin Cancer Res*. 2020;26(22):5943-5951. <https://doi.org/10.1158/1078-0432.CCR-20-1804>
- Beshiri ML, Tice CM, Tran C, et al. A PDX/organoid biobank of advanced prostate cancers captures genomic and phenotypic heterogeneity for disease modeling and therapeutic screening. *Clin Cancer Res*. 2018;24(17):4332-4345. <https://doi.org/10.1158/1078-0432.CCR-18-0409>
- Shi H, Tao T, Abraham BJ, et al. ARID1A loss in neuroblastoma promotes the adrenergic-to-mesenchymal transition by regulating enhancer-mediated gene expression. *Sci Adv*. 2020;6:1-12.
- Jung EM, Moffat JJ, Liu J, Dravid SM, Gurumurthy CB, Kim WY. Arid1b haploinsufficiency disrupts cortical interneuron development and mouse behavior. *Nat Neurosci*. 2017;20(12):1694-1707. <https://doi.org/10.1038/s41593-017-0013-0>
- La Manno G, Soldatov R, Zeisel A, et al. RNA velocity of single cells. *Nature*. 2018;560(7719):494-498. <https://doi.org/10.1038/s41586-018-0414-6>
- Biddy BA, Kong W, Kamimoto K, et al. Single-cell mapping of lineage and identity in direct reprogramming. *Nature*. 2018;564(7735):219-224. <https://doi.org/10.1038/s41586-018-0744-4>
- Gao R, Bai S, Henderson YC, et al. Delineating copy number and clonal substructure in human tumors from single-cell transcriptomes. *Nat Biotechnol*. 2021;39(5):599-608. <https://doi.org/10.1038/s41587-020-00795-2>
- Joseph DB, Turco AE, Vezina CM, Strand DW. Progenitors in prostate development and disease. *Dev Biol*. 2021;473:50-58.
- Taavitsainen S, Engedal N, Cao S, et al. Single-cell ATAC and RNA sequencing reveal pre-existing and persistent cells associated with prostate cancer relapse. *Nat Commun*. 2021;12(1):5307. <https://doi.org/10.1038/s41467-021-25624-1>
- Cheng Q, Butler W, Zhou Y, et al. Pre-existing castration-resistant prostate cancer-like cells in primary prostate cancer promote resistance to hormonal therapy. *Eur Urol*. 2022;81(5):446-455. <https://doi.org/10.1016/j.eururo.2021.12.039>
- Han H, Wang Y, Curto J, et al. Mesenchymal and stem-like prostate cancer linked to therapy-induced lineage plasticity and metastasis. *Cell Rep*. 2022;39(1):110595. <https://doi.org/10.1016/j.celrep.2022.110595>
- Karthaas WR, Hofree M, Choi D, et al. Regenerative potential of prostate luminal cells revealed by single-cell analysis. *Science*. 2020;368(6490):497-505. <https://doi.org/10.1126/science.aay0267>
- Tang F, Xu D, Wang S, et al. Chromatin profiles classify castration-resistant prostate cancers suggesting therapeutic targets. *Science*. 2022;376(6596):eabe1505. <https://doi.org/10.1126/science.abe1505>
- Chan JM, Zaidi S, Love JR, et al. Lineage plasticity in prostate cancer depends on JAK/STAT inflammatory signaling. *Science*. 2022;377(6611):1180-1191. <https://doi.org/10.1126/science.abn0478>
- Bishop JL, Thaper D, Vahid S, et al. The master neural transcription factor BRN2 is an androgen receptor-suppressed driver of neuroendocrine differentiation in prostate cancer. *Cancer Discov*. 2017;7(1):54-71. <https://doi.org/10.1158/2159-8290.CD-15-1263>
- Cejas P, Xie Y, Font-Tello A, et al. Subtype heterogeneity and epigenetic convergence in neuroendocrine prostate cancer. *Nat*

- Commun.* 2021;12(1):5775. <https://doi.org/10.1038/s41467-021-26042-z>
32. Dardenne E, Beltran H, Benelli M, et al. N-Myc induces an EZH2-mediated transcriptional program driving neuroendocrine prostate cancer. *Cancer Cell.* 2016;30(4):563-577. <https://doi.org/10.1016/j.ccell.2016.09.005>
 33. Perez Kerkvliet C, Dwyer AR, Diep CH, et al. Glucocorticoid receptors are required effectors of TGFbeta1-induced p38 MAPK signaling to advanced cancer phenotypes in triple-negative breast cancer. *Breast Cancer Res.* 2020;22(1):39. <https://doi.org/10.1186/s13058-020-01277-8>
 34. Fennell KA, Vassiliadis D, Lam EYN, et al. Non-genetic determinants of malignant clonal fitness at single-cell resolution. *Nature.* 2021;601(7891):125-131. <https://doi.org/10.1038/s41586-021-04206-7>
 35. Bolis M, Bossi D, Vallergera A, et al. Dynamic prostate cancer transcriptome analysis delineates the trajectory to disease progression. *Nat Commun.* 2021;12(1):7033. <https://doi.org/10.1038/s41467-021-26840-5>
 36. Davies A, Nouruzi S, Ganguli D, et al. An androgen receptor switch underlies lineage infidelity in treatment-resistant prostate cancer. *Nat Cell Biol.* 2021;23(9):1023-1034. <https://doi.org/10.1038/s41556-021-00743-5>
 37. Glover DM, Leibowitz MH, McLean DA, Parry H. Mutations in aurora prevent centrosome separation leading to the formation of monopolar spindles. *Cell.* 1995;81:95-105.
 38. Eterno V, Zambelli A, Villani L, et al. Aurka controls self-renewal of breast cancer-initiating cells promoting wnt3a stabilization through suppression of miR-128. *Sci Rep.* 2016;6:28436. <https://doi.org/10.1038/srep28436>
 39. Du J, Jing J, Chen S, et al. Arid1a regulates cell cycle exit of transit-amplifying cells by inhibiting the Aurka-Cdk1 axis in mouse incisor. *Development.* 2021;148(8):dev198838. <https://doi.org/10.1242/dev.198838>